Journal of Materials Science & Technology 251 (2026) 297–310

Contents lists available at ScienceDirect

Journal of Materials Science & Technology

journal homepage: www.elsevier.com/locate/jmst

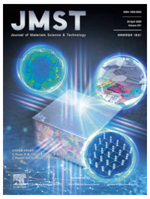

Research Article

Efficient preparation of strong and tough 304 stainless steels via high-frequency pulse forging

Weiheng Xia[a], Jiaqi Meng[a], Runchang Liu[a], Zongyao Li[a], Yang Cao[a,b,*], Yonghao Zhao[a,b,*]

[a] *Nano and Heterogeneous Materials Center, School of Materials Science and Engineering, Nanjing University of Science and Technology, Nanjing 210094, China*

[b] *School of Materials Science and Engineering, Hohai University, Changzhou 213200, China*

ARTICLE INFO

Article history:
Received 22 April 2025
Revised 22 June 2025
Accepted 30 June 2025
Available online 29 July 2025

Keywords:
Austenitic stainless steel
Rotary swaging
Martensite transformation
Annealing hardening
Nanoscale precipitates

ABSTRACT

In this paper, a commercial grade 304 SS has been processed by high-frequency pulse forging - rotary swaging (RS) to different strains up to 1.5. The average grain size, volume fraction of martensite and total dislocation density of ~80 nm, 68 vol.% and 2.15×10^{15} m^{-2}, respectively, are achieved in the 304 steel at an equivalent strain of ~1.5, granting the steel withan ultra-high yield strength of 2235 MPa. Subsequent annealing at 450 °C for 10 min, led to the unexpected formation of high-density B2 nanoprecipitates for the first time in the 304 steel and an increased volume fraction of nanostructured martensite, and thus further increased the yield strength to a new record of 2375 MPa. Annealing the RS steel at 700 °C for 10 min, led to the heterostructure consisting of coarse-grained austenite, nanostructured austenite and nanostructured martensite. Semi-in-situ X-ray diffraction tensile tests, in-situ digital image correlation analysis and ex-situ microstructural characterization together reveal that the heterostructured 304 steel deforms via synergistic deformation mechanisms involving martensitic transformation, deformation twinning, dislocation-precipitate interactions, thus demonstrating the excellent yield strength of 1290 MPa and uniform elongation of 20.1 %.

1. Introduction

Austenitic stainless steels have been used in nearly all industries, including aerospace, nuclear power, petroleum, automobile, biomedical, food processing, textile manufacturing, etc. [1–3], owing to their excellent corrosion resistance, formability, workability, weldability and non-magnetic property [4–8]. Austenitic stainless steels usually have large contents of chromium and nickel which stabilize the austenitic phase at room temperature and provide the steels with excellent corrosion resistance, but on the other hand significantly lower the yield strength (YS). Fortunately, austenitic stainless steels do have widely adjustable mechanical properties due to their comparatively low stacking fault energies (SFE) and the associated propensity for twinning and martensitic transformation [9]. Both twinning and martensitic transformation can accommodate plastic strain by shearing on slip planes, which are known as the twin-induced plasticity [10] and transformation-induced plasticity [11], respectively. Once twins and martensite form, they can provide excess boundaries for blocking and storing dislocations, and thus significantly improve the strength at the cost of ductility. Nevertheless, common boundary strengthening mechanisms such as high and low angle boundary strengthening can also be easily realized in austenitic stainless steels via cold plastic deformation to sufficiently high strains [12].

Austenitic stainless steels are high alloy steels, typically containing multiple alloying elements, including minor/trace additions, with the total alloying content exceeding 20 wt. %. The high alloying contents grant the steels with possibility of solute segregation and precipitation upon heat treatment. Recently, strengthening by introducing coherent nanoprecipitates in steels and multi-principal element alloys has received much attention [13]. Knowing that combining the processes of severe plastic deformation (SPD) and heat treatment can change the precipitation kinetics in many alloys [14], we are therefore wondering if some sort of beneficial precipitates can also be made in industrial-grade austenitic steels via readily available industrial processes. Strengthening of plastically deformed austenitic stainless steels after low-temperature annealing has been reported [15,16]. The strengthening phenomenon has been attributed to annealing-induced martensitic transformation [15] or significant recovery of mobile dislocations [16]. In our present study, following low-temperature annealing, we ob-

---

[*] Corresponding authors.
E-mail addresses: y.cao@hhu.edu.cn (Y. Cao), yhzhao@njust.edu.cn (Y. Zhao).

https://doi.org/10.1016/j.jmst.2025.06.051
1005-0302/

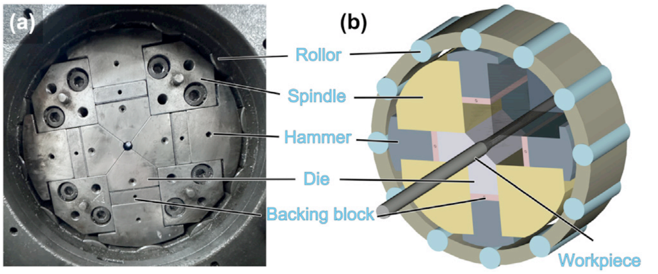

Fig. 1. (a) Structural components of the RS system; (b) schematic illustration of the RS setup.

served not only an increase in martensite content but also the precipitation of nano-sized B2 phase. This marks the first report of nano-sized B2 phase, typically found in Al-rich steels [17–19] and in an Al-free 304 steel. As a potent strengthening phase, the B2 phase contributes to strengthening in materials such as Al-containing lightweight steels, maraging steels, and medium-Mn steels [17,19,20]. Our findings provide an alternative explanation for annealing-induced strengthening in austenitic steels and offer a new insight for designing high-strength austenitic steels.

Both martensite and precipitate are secondary phases with distinct mechanical properties from the austenitic matrix. According to the pioneering work by Wu et al. [21], the existence of heterogeneous zones such as dual phase structure and precipitate-matrix structure may stimulate hetero-deformation induced (HDI) strengthening effect [22] on top of conventional strain hardening effect to help optimize the strength-ductility combination in metallic materials. Encouragingly, there have already been some reports on heterostructured steels with improved mechanical properties [23], thus opening the horizon for making better austenitic stainless steels with heterostructures. Romero-Resendiz et al. systematically reviewed the deformation mechanisms and properties of heterostructured stainless steel, providing valuable knowledge that supports our current work [24].

While having many materials strengthening concepts in mind, we urgently need to put the concepts into practice and find the processing route for making ultra-strong austenitic stainless steels at an industrial scale. Severe plastic deformation [25] processes can theoretically impose unlimited strains for achieving the ultimate boundary strengthening effect to even triple the strength of steels [26], but high costs and scaling-up of the SPD processes are still unsolved issues. Conventional plastic deformation processes such as rolling and extrusion are widely used for mass production of steel products, but the work hardening effect is limited due to low strain input and low strain rate [27].

Rotary swaging (RS) is a near-net metal forming process that uses high-speed pulse hammers/dies to strike a cylindrical workpiece such as a solid rod or hollow tube, while the workpiece is axially fed into the unit of swaging dies, as shown in Fig. 1. RS has following characteristics: (1) High-frequency pulse impact loading: 12 or more pressure rollers are radially distributed around a full set of hammer blocks and dies (Fig. 1(b)); therefore, each full rotation of the forging dies can forge the sample 12 times or more; by adjusting the rotation speed, the swaging machine using four dies can produce 180–1700 strokes per minute. (2) Multi-direction forging: the sample is forged/formed by four radially placed dies, therefore, the cylindrical sample experiences compressive strain in radial directions and tensile strain in the axial direction, simultaneously. The multi-directional strains and stresses are effective in activating multiple slip systems for dislocations and even twinning. (3) High strain rate: it takes only 0.04 s or less for a swaging machine to produce a complete stroke; by using different sets of dies and spacers, the strain rate can be adjusted from 1 to 100 s^{-1}. (4) Low strain input: the equivalent strain imposed by each strike is only 0.01 or even much lower; such low strain input can help prevent premature failure and cracking during the swaging process, and control the shape and surface quality of the workpiece. (5) Applicable to a wide range of metals: RS can efficiently reduce, taper, shape, form, or bond metal parts by imposing complex three-dimensional stress states and incremental strains, even for metals with low ductility such as magnesium alloys and metals with high strength such as tungsten, molybdenum and nickel alloys.

Nowadays, RS is already a widely used industrial metal processing method that can continuously process a workpiece with theoretically unlimited length. RS has low cost and high production efficiency, making it especially suitable for mass production. Although the plastic strain imposed by RS may not be as large as the SPD methods, the high strain rate imposed by RS in the radial direction can drastically increase the dislocation densities in the metal workpiece for effective strain hardening. There have already been many studies recently reporting the successful conduct of RS [28,29] for processing high-strength Ti [30], Mg-Gd-Y-Zr and AZ31 alloys [31–33], high-conductivity Cu and Cu-Cr alloys [34–36], high-toughness Al matrix composites [37–39], etc. Hence, we are keen to prove the feasibility of making high-strength austenitic stainless steels by RS, and to understand the underlying co-action of various strengthening mechanisms.

2. Experimental

2.1. Rotary swaging and heat treatment

The 304 grade steels have ~18 % Cr and ~8 % Ni and are therefore also known as 18/8 stainless steel. It has comparable mechanical properties and costs much <316 grade steels, and thus makes it an excellent choice of model materials. The composition of the model material is provided in Table 1. The as-received 304 stainless steel (304 SS) has a uniform microstructure with an average grain size of 13.1 µm, as shown in Fig. 2(a) and (b). Fig. 2(c) shows a schematic diagram of the RS process. The 304 SS bar with an initial diameter of 24 mm and a length of 1 m underwent RS at room temperature. RS reduced the diameter of the bar to 18.7, 14.6 and 11.3 mm, corresponding to the equivalent strains of 0.5, 1 and 1.5, respectively, as shown in Fig. 2(d). The RS processed 304 SS samples are named RS0.5, RS1 and RS1.5 hereafter. The equivalent strain was calculated by the formula, $\varepsilon = \ln(A_0/A)$, where A_0 and A are the initial and post-swaging cross-sectional areas, respectively. The RS1.5 samples were annealed for 10 min in a muffle furnace at temperatures of 450 and 700 °C. The annealed samples are named RS-450 and RS-700, respectively (Fig. 3).

2.2. Mechanical property tests

As shown in Fig. 3, the flat dog-bone shaped samples for tensile tests have the gauge length, width and thickness of 10, 2.5 and 1 mm, respectively. The tensile samples were cut from the bars by the electrical spark wire cutting machine. The surfaces and edges of the tensile samples were polished with 320#, 1000# and 2000# sandpapers to remove surface impurities and scratch marks. Uniaxial quasi-static tensile tests were conducted by the Walter+bai LFM 20 kN tensile test machine equipped with an Epsilon contact extensometer, to measure mechanical properties of the steel samples under the tensile strain rate of 1×10^{-3} s^{-1}. Tensile tests were repeated at least three times for each sample to ensure reliability.

2.3. Microstructural characterization

Microstructural characterization was carried out by means of electron back-scattered diffraction (EBSD) and transmission elec-

Table 1
Chemical compositions of the 304 SS used in the present study (wt. %).

C	Si	Mn	P	S	Ni	Cr	Mo	N	Fe
0.046	0.41	1.12	0.027	0.01	8.08	17.51	0.14	0.035	Bal.

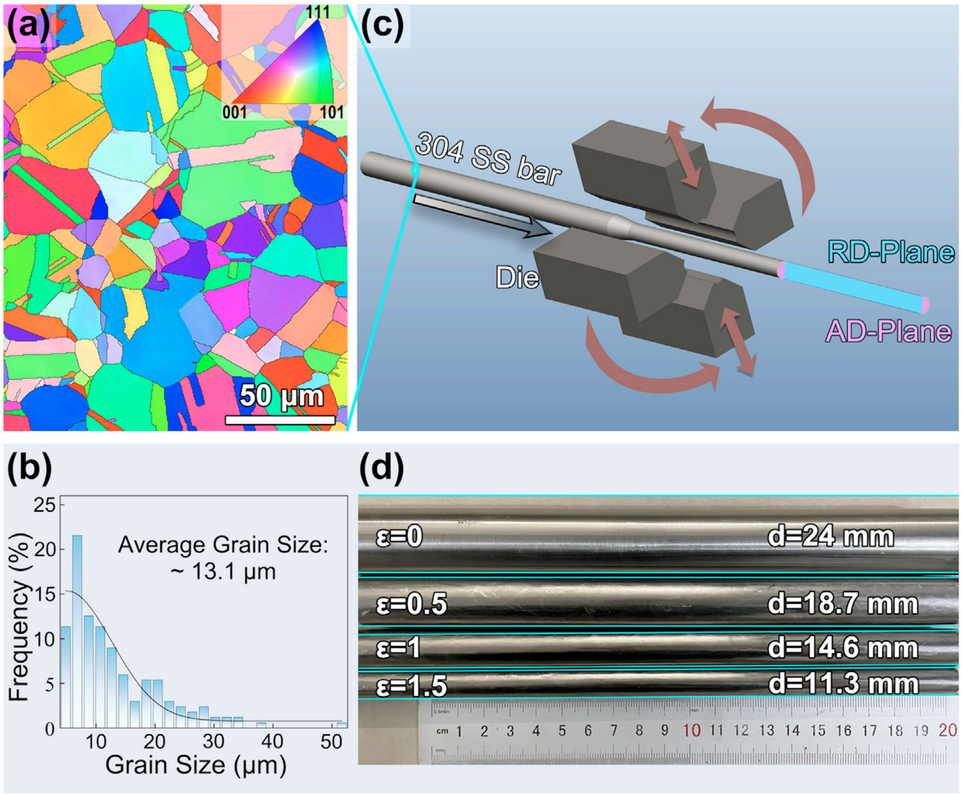

Fig. 2. (a) EBSD inverse pole figure (IPF) map of the as-received 304 SS sample, and (b) corresponding grain size distribution chart. (c) Schematic illustration of the RS process. (d) 304 SS bars before and after RS.

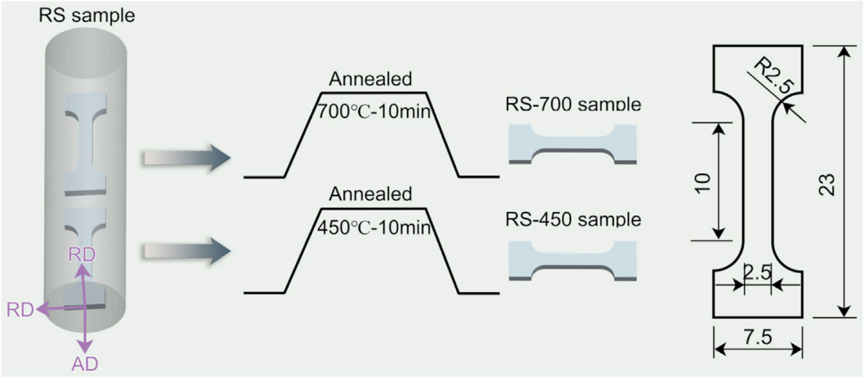

Fig. 3. Heat treatment process diagram, and dimensions of the dog-bone shaped sample for tensile tests (Unit: mm). The samples are defined by the coordinate system with the axial direction (AD) and radial direction (RD).

tron microscopy (TEM) techniques. All EBSD samples were mechanically polished and subsequently electro-polished for a mirror finish. The electrolytic polishing solution is a mixture of 25 % perchloric acid and 75 % glacial acetic acid. EBSD mapping was conducted by using a high-resolution field emission Carl Zeiss-Auriga-45–66 scanning electron microscope (SEM) equipped with a fully automatic Oxford Instruments Aztec 2.0 EBSD system (Channel 5 software). The acceleration voltage of 20 kV and working distance of 14–16 mm were used for EBSD acquisition. The step size of 40 nm was used for EBSD analysis.

The TEM sample preparation has been done by the following procedures: thin slices with the thickness of ~0.6 mm were cut by electrical spark wire cutting, and then ground to the thickness of ~100 μm with 600#, 1000#, 1500# sandpapers in turn; thin disks with the diameter of 3 mm were punched off the thin slices, and then further ground to the thickness of ~60 μm with the 2000# sandpaper; finally, perforations were done to the thin disks by electro-polishing with the electrolyte solution containing 25 vol. % perchloric acid and 75 vol. % glacial acetic acid, under the applied voltage of ~15 V. TEM observations have been carried

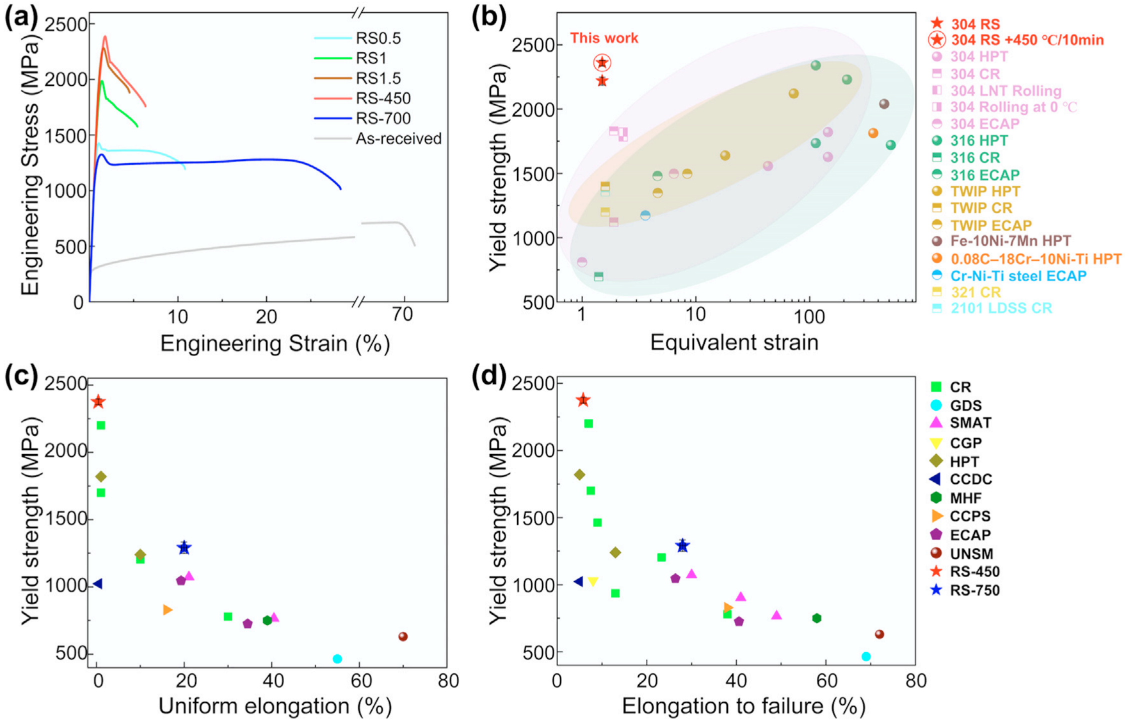

Fig. 4. (a) Engineering stress-strain curves for the 304 SS samples processed under different conditions in the present study. (b) Relationship between yield strength and the equivalent strain imposed by various plastic deformation methods. (c) Yield strength versus uniform elongation for the 304 SS processed by different methods. (d) Yield strength versus elongation to failure for 304 SS processed by different methods. The statistical data are obtained from the present study and literature [16,26,42–73].

out on FEI Tecnai 20 LaB6 high-resolution TEM (200 kV) and FEI Titan spherical aberration corrected high-resolution TEM (HR-TEM) operating at 300 kV. High-resolution energy-dispersive X-ray spectroscopy (EDS) analysis was done by a double Cs-corrected Grand ARM 300F TEM operating at 300 kV.

X-ray diffraction (XRD) experiments were performed using the Bruker AXS D8 Advance diffractometer, which has the Cu target K_{α} radiation with a wavelength of 0.15406 nm. The acceleration voltage is 40 kV, the current is 40 mA, and the scanning angle ranges 40°–100°. The XRD line profiles are recorded with a step size of 0.02° and a dwell time of 1 s. The volume fractions of austenite and α'-martensite were deduced from the XRD data with Eq. (1) [40]:

$$V_{\alpha'} = \frac{\frac{1}{n}\sum_{j=1}^{n}\frac{I_{\alpha'}^{j}}{R_{\alpha'}^{j}}}{\frac{1}{n}\sum_{j=1}^{n}\frac{I_{\gamma}^{j}}{R_{\gamma}^{j}} + \frac{1}{n}\sum_{j=1}^{n}\frac{I_{\alpha'}^{j}}{R_{\alpha'}^{j}}} \tag{1}$$

where $V_{\alpha'}$ is the volume fraction of α'-martensite. R and I are the theoretical intensities and integrated intensities for (*hkl*) planes, respectively [41]. n is the number of peaks examined.

3. Results

3.1. Mechanical properties

The engineering stress-strain curves for the 304 SS samples processed under different conditions are shown in Fig. 4(a). Correspondingly, the mechanical properties, including YS, ultimate tensile strength (UTS), uniform elongation (UE) and elongation to failure (FE), are summarized in Table 2. As shown in Fig. 4(a), the RS process is very effective in producing work hardening effect to the 304 SS samples. An equivalent strain of 0.5 is sufficient to elevate the YS of the 304 SS to 1415 MPa, which is five times higher than the as-received sample. As the RS imposed strain increased further to 1 and 1.5, the YS of the 304 SS continued to increase to 1819 and 2235 MPa, respectively. After annealing the RS1.5 sample for 10 min at 450 °C, the YS strength was further increased to a record high of 2375 MPa, which is more than eight times stronger than a commercial coarse-grained 304 SS. After annealing the RS1.5 sample at 700 °C for 10 min, the RS-700 sample with an excellent combination of strength (YS = 1290 MPa) and ductility (UE = 20.1 %) is made.

Table 2
Tensile properties of the as-received, RS-treated, and annealed 304 SS.

Sample	YS (MPa)	UTS (MPa)	UE (%)	FE (%)
As-received	297 ± 20	727 ± 20	65.1 ± 5.2	69.3 ± 2.3
RS0.5	1415 ± 10	1424 ± 11	0.2 ± 0.1	10.9 ± 1.3
RS1	1819 ± 32	1961 ± 41	0.3 ± 0.1	5.1 ± 0.4
RS1.5	2235 ± 30	2293 ± 13	0.4 ± 0.1	3.4 ± 0.9
RS-450	2375 ± 21	2395 ± 13	0.4 ± 0.2	5.8 ± 0.6
RS-700	1290 ± 42	1299 ± 26	20.1 ± 0.6	28.18 ± 0.3

Fig. 4(b) shows the relationship between yield strength and the processing strain for a series of representative austenitic steels. The steel grade is distinguished by colors, and the processing method is distinguished by point shapes. Although the concurrent evolution of dislocation structures and grain refinement process under plastic deformation demonstrates stochastic and intermittent dynamics [74], the dislocation density increases and the grain size decreases with the increasing strain, which is still the general trend. While the dislocation and Hall-Petch strengthening effects govern the strength of the steels, the yield strength of the steels increases with increasing strain, as the general trend is reasonably shown in Fig. 4(b). Conventional cold working methods, such as cold rolling (CR), can hardly impose a strain larger than 5, even by the aid of liquid nitrogen temperature, the strength of 304 steel can only be increased to 1820 MPa [42,43]. Some 316 steels processed by high-pressure torsion (HPT) can have the yield strength

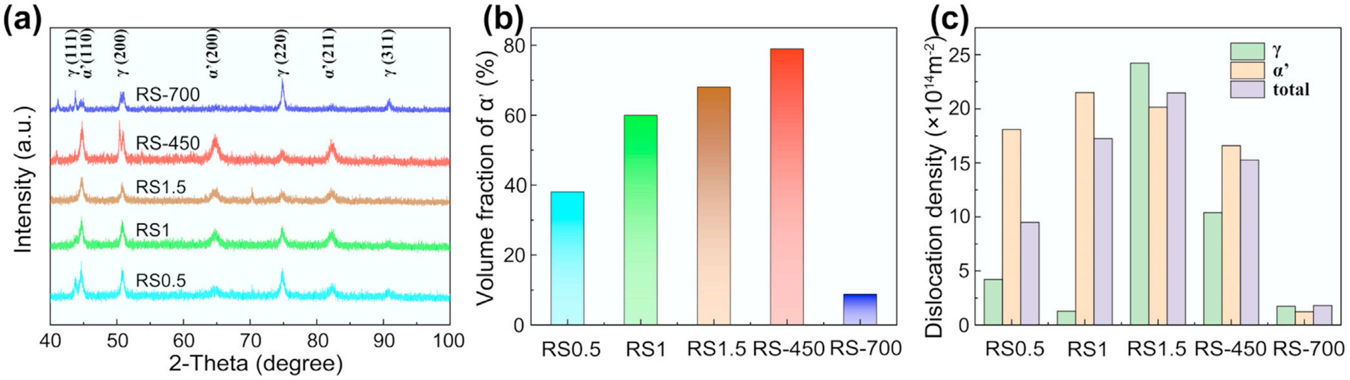

Fig. 5. (a) XRD patterns of the samples treated with different RS strains and annealing temperatures, and (b) volume fractions of α' phase deduced from the XRD patterns in (a). (c) Dislocation densities in the steel samples processed by different conditions.

increased above 2000 MPa, but the sample size is limited to a coin piece. Considering only a moderate strain of 1.5 and short-time annealing of 10 min at 450 °C were done to the 304 SS, the strengthening effect is stunning. Especially, as shown by the "red stars" in Fig. 4(b–d), the YS of RS-450 °C sample has reached a new record high of 2375 MPa surpassing all other 304 SS processed by other cold working methods including CR [44], cyclic torsion (CT) [45], surface mechanical rolling treatment (SMRT) [46], constrained groove pressing (CGP) [47], HPT [48], cyclic channel die pressing (CCDC) [49], multi-directional hot forging (MHF) [50], cryogenic cyclic plastic strengthening (CCPS) [51], equal-channel angular pressing (ECAP) [52] and ultrasonic nanocrystal surface modification (UNSM) [53]. Annealing the RS1.5 sample at 700 °C for only 10 min, significantly improved the ductility at the expense of strength, pushing the combination of strength and ductility slightly beyond the "banana curves" as shown by the "blue stars" in Fig. 4(c) and (d).

3.2. Microstructure

As shown in Fig. 5(a), XRD peaks for both austenite with the face-centered cubic (FCC) structure and martensite with the body-centered tetragonal (BCT) structure [75,76] are apparent in all RS processed samples. With the increase of strain, the intensities of austenite peaks decrease, while the intensities of martensite peaks increase. After annealing the RS1.5 sample at 450 °C for 10 min, the intensities of the martensite peaks in the RS-450 sample increased even higher. After annealing at 700 °C for 10 min, the intensities of the martensite peaks for the RS-700 sample decreased compared to the RS-450 sample. The volume fractions of martensite are deduced from the XRD patterns in Fig. 5(a) and shown in Fig. 5(b). As the RS strain increased from 0.5 to 1.5, the volume fractions of martensite increased from 38 % to 68 %; for the RS-450 sample, the volume fraction of martensite increased even further to 79 %. Considering that the martensitic phase is metastable, annealing the RS1.5 sample at 700 °C expectedly reduced the volume fraction of martensite to 8.8 %.

Fig. 5(c) shows dislocation densities in the 304 SS samples processed under different conditions. In the RS0.5 and RS1 samples, the dislocation densities (green bars) in austenite are 4.21 $\times$ 10^{14} m^{-2} and 1.28 $\times$ 10^{14} m^{-2}, respectively, which are significantly lower than the dislocation densities in martensite (wheat bars). When the RS strain is increased to 1.5, both austenite and martensite possess high dislocation densities above 2 $\times$ 10^{15} m^{-2}. It has been reported that martensitic transformation in 304 steels reduces the local strain energy [76]. Therefore, we suspect that martensitic transformation has consumed a large number of dislocations in the austenite. However, when the grain size is reduced to the ultrafine grain region and the volume fractions of martensite increases to a very high level, for example in the case of RS1.5 sample, the dislocation density in the austenite increased drastically to 2.42 $\times$ 10^{15} m^{-2}, in response to the high flow stress and large strain gradients at austenite/martensite interfaces. Annealing the RS1.5 sample at 450 °C for 10 min, moderately reduced the dislocation densities in both austenite and martensite in the RS-450 sample, but the dislocation densities in austenite decreased faster than in martensite. Annealing the RS1.5 sample at 700 °C for 10 min, reduced the dislocation densities in austenite and martensite to 1.74 $\times$ 10^{14} and 1.22 $\times$ 10^{14} m^{-2}, respectively, in the RS-700 sample.

Semi-in-situ XRD tensile tests and digital image correlation (DIC) tensile analysis were conducted on the RS-700 sample, which possesses an excellent combination of strength and ductility. As shown in Fig. 6(a), the XRD peaks for both austenite and martensite co-exist when the tensile strain is 2 %, but the martensite peak at 44.8° is weak. As the tensile strain increases to 8 % and 14 %, almost all of the martensite peaks increase and all of the austenite peaks decrease correspondingly. When the tensile strain increases to 20 %, the austenite peaks at 43.6° and 90.7° almost disappear.

The volume fractions of martensite increase with the tensile strain for the RS-700 sample, as shown in Fig. 6(b). The engineering stress-strain curve and snap shots of DIC strain contour maps are also shown in Fig. 6(b), to help illustrate the correlation between tensile deformation and martensitic transformation in the RS-700 sample. When the RS-700 sample was tensile deformed from 0 % to 2 % elongation, the stress first increased to a peak value of 1323.8 MPa and then dropped slightly to 1230.8 MPa. Correspondingly, the volume fraction of martensite was increased from 8.8 % to 18.5 %. At the tensile strain of 2 %, when the stress/yield began to level off, a narrow band of strain localization in the color of sky blue formed in the strain contour map. As the tensile strain increased from 2 % to 8 %, the fraction of martensite increased linearly from 18.5 % to 49.0 %, and correspondingly the high strain region expanded from the lower part of the sample towards the upper part of the sample, in the way similar to the expansion of Lüders band [77]. As the tensile strain increased from 8 % to 14 %, the fraction of martensite increased linearly from 49.0 % to 63.6 % with a slightly reduced slope, and yellow color dispersive strain bands spread over the whole gauge section. As the tensile strain increased from 14 % to 20 %, the fraction of martensite continued to increase linearly from 63.6 % to 75.7 %, and the necking region began to form at the central part of the tensile sample. A plateau of the stress-strain curve is seen in the tensile strain range from 2 % to 20 % in conjunction with the near-linear increase in the fraction of martensite. Meanwhile, the dislocation densities in both austenite and martensite increase with increas-

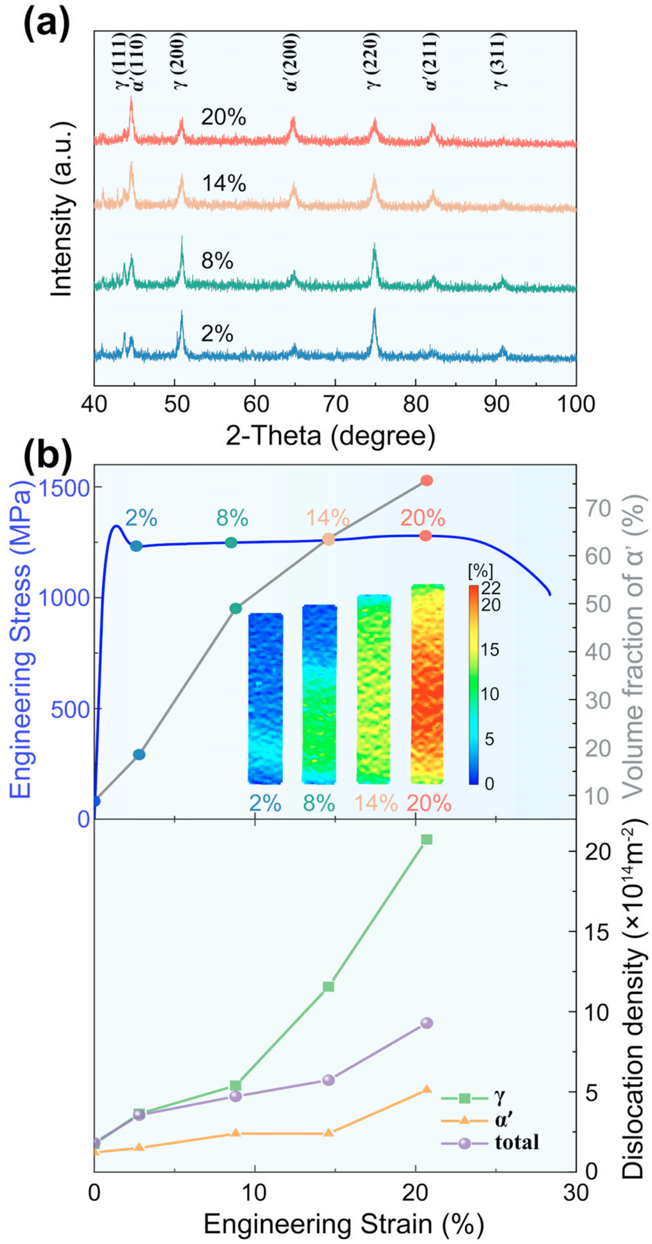

Fig. 6. (a) XRD patterns of the RS-700 sample deformed to different tensile strains. (b) Engineering stress-strain curve for the RS-700 sample; the variation of volume fractions of martensite as a function of strain; DIC strain contour maps obtained at different tensile strains; dislocation density evolutions with respect to tensile strain.

ing tensile strain, demonstrating the strain hardening effect. It shall be noticed that the dislocation density in austenite increases much faster than in martensite; this is due to the HDI strengthening effect that the soft austenite requires a high density of geometrically necessary dislocations (GNDs) to accommodate the strain gradients at austenite/martensite interfaces [78].

Fig. 7(a) shows the heterogeneous grains structure consisting of a large number fraction of ultrafine grains and a small number fraction of coarse grains in the RS-700 sample. All coarse grains and the majority of the ultrafine grains are the austenitic phase due to annealing-induced reverse martensitic transformation [79], as shown in Fig. 7(b). Although the RS-700 sample has been annealed at a high temperature of 700 °C, there are still 62.7 % of the grains been recognized as deformed grains, as shown in Fig. 7(c). This is because short-time annealing for 10 min is insufficient to recover the dislocations associated with reverse martensitic transformation. The deformed and recrystallized grains are heterogeneously distributed throughout the bulk sample (Fig. 7(a)) and are closely related to the heterogeneous distribution of the coarse and ultrafine grains (Fig. 7(c)). All of the red Σ3 twin boundaries in Fig. 7(b) are located in the regions of recrystallized grains in Fig. 7(c), suggesting that they are annealing twins (ATs). The EBSD-based statistical result in Fig. 7(d) shows that the average grain size is approximately 200 nm in the RS-700 sample. The misorientation distribution chart in Fig. 7(e) shows two peaks, one at low angles and the other at ~60°. The large fraction of low-angle boundaries is related to the deformed grains and substructures. The peak at ~60° is related to the Σ3 twin boundaries.

The RS-700 sample was tensile deformed to fracture. The fracture tip is analyzed by EBSD, and the result is shown in Fig. 8. The hit-rate of EBSD detection is comparatively low due to high densities of accumulated dislocations, leaving many unresolved black areas throughout the EBSD maps as shown in Fig. 8(a) and (b). Austenite grains are hardly seen in Fig. 8(a), indicating that martensitic transformation is the major plastic strain carrier for the tensile deformation, and has occurred throughout the fracture tip region.

In order to capture the microstructural details beyond the resolution of SEM and EBSD, TEM observations have been done on RS samples, RS plus annealing samples and tensile deformed samples. Fig. 9 shows the microstructures of the 304 SS samples deformed by RS to strains of 0.5, 1, and 1.5. In the RS0.5 sample, thin bands which are deformation twins and/or martensite [80] can be observed on both AD-plane (Fig. 9(a1)) and RD-plane (Fig. 9(a2)), suggesting that twinning and/or martensitic transformation are active in multiple slip systems. In the RS1 sample, dislocation substructures and sub-grains of irregular shapes are seen on the AD-plane (Fig. 9(b1)). Thin band structures inclined to the AD direction are seen on the RD-plane (Fig. 9(b2)). In the RS1.5 sample, some equiaxed sub-grains with shape boundaries are seen on the AD-plane (Fig. 9(c1)). Elongated sub-grains nearly parallel to the AD direction are seen on the RD-plane (Fig. 9(c2)). The average size of the equiaxed sub-grains observed on the AD-plane is approximately 80 ± 51 nm which matches the average thickness of the elongated sub-grains observed on the RD-plane. As shown in Fig. 9(d1) and (d2), the selected area electron diffraction (SAED) rings corresponding to α'-martensite are much brighter than the SAED rings corresponding to γ-austenite. The brightness of the SAED patterns is consistent with the XRD result, and the volume fraction of martensite is much larger than that of the austenite in the RS1.5 sample. Based on the TEM images in Fig. 9, it can be concluded that significant grain refinement has been achieved via cooperative deformation [14] involving twinning, martensitic transformation, dislocation entanglement, and dislocation-boundary interactions. The resultant sub-grains are elongated along the AD direction to accommodate the elongation of the bulk sample.

The RS-450 sample is made by annealing the RS1.5 sample at 450 °C for 10 min. The RS-450 sample consists of nanograins, ultrafine grains and dislocation substructures as shown in Fig. 10(a). Bright SAED rings for α'-martensite and dull rings for γ-austenite are observable from the inset in Fig. 10(a), supporting the XRD-measured large fraction of martensite. The sub-grains viewed on the RD-plane show elongation parallel to the AD, as shown in Fig. 10(b). The contrast varies along the long axis of the grains, indicating the rich content of dislocations and substructures in the grains. Well-developed nano-grains are hardly found. Therefore, annealing at 450 °C for 10 min was insufficient to cause inverse martensitic transformation or recrystallisation in the RS processed nanostructured 304 SS.

Fig. 10(c) and (f) presents bright-field TEM images viewed on AD-plane and RD-plane, respectively, in which ultrafine sub-grains

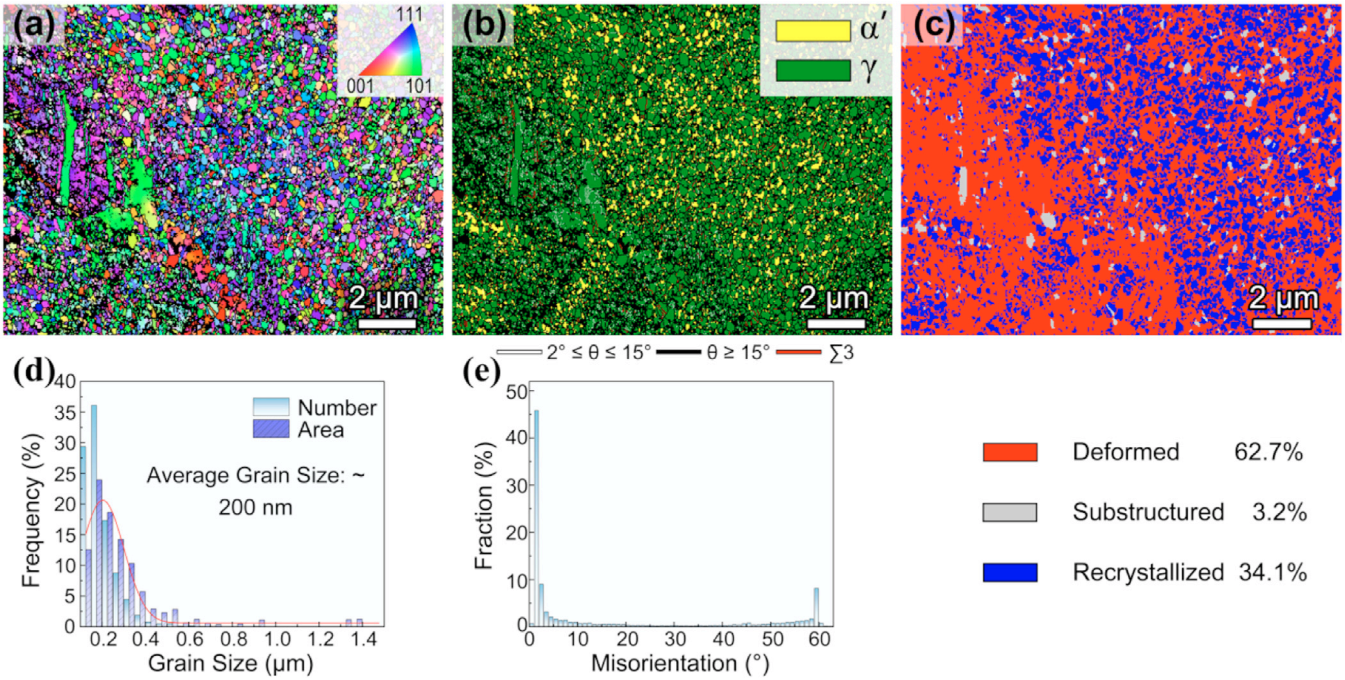

Fig. 7. Microstructure of the RS-700 sample: (a) EBSD IPF map; (b) EBSD map showing phases and grain boundaries; (c) EBSD map showing deformed grains, recrystallized grains and dislocation substructures; (d) grain size distribution chart; (e) grain boundary misorientation distribution chart.

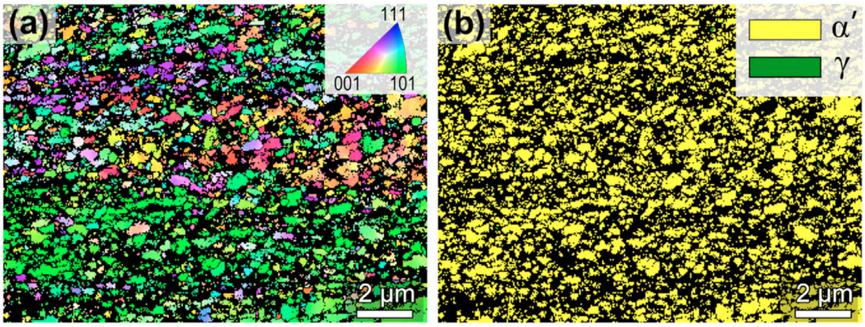

Fig. 8. Microstructure of the RS-700 sample at tensile fracture: (a) EBSD IPF map and (b) EBSD phase map.

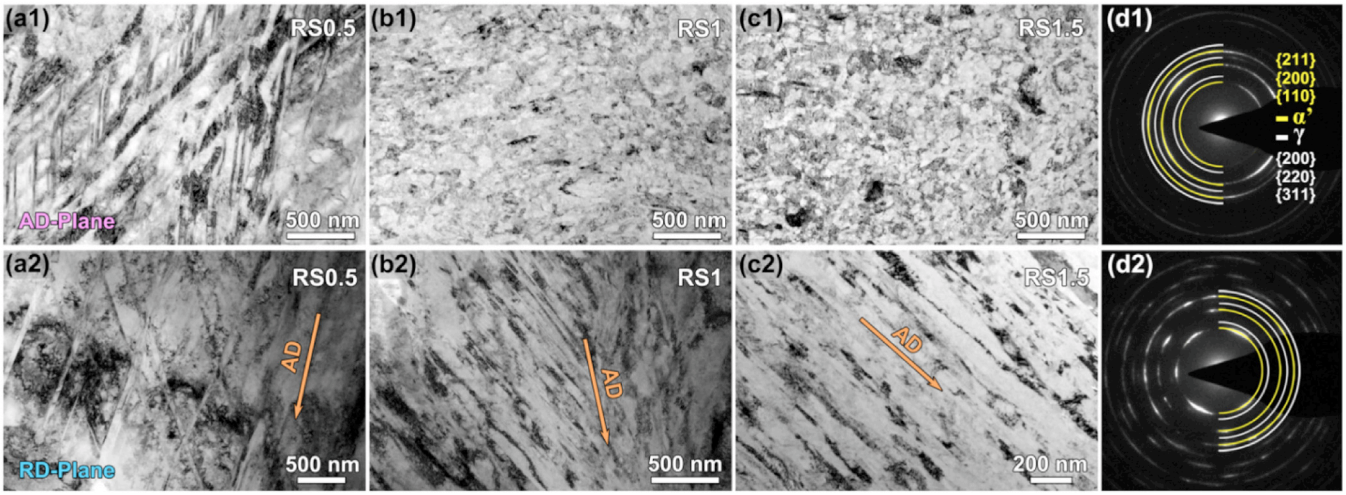

Fig. 9. Bright-field TEM images of (a1, a2) RS0.5, (b1, b2) RS1 and (c1, c2) RS1.5 samples. (a1–c1) are observed from AD-Planes; (a2–c2) are observed from RD-Planes. (d1) SAED pattern corresponding to (c1); (d2) SAED pattern corresponding to (c2).

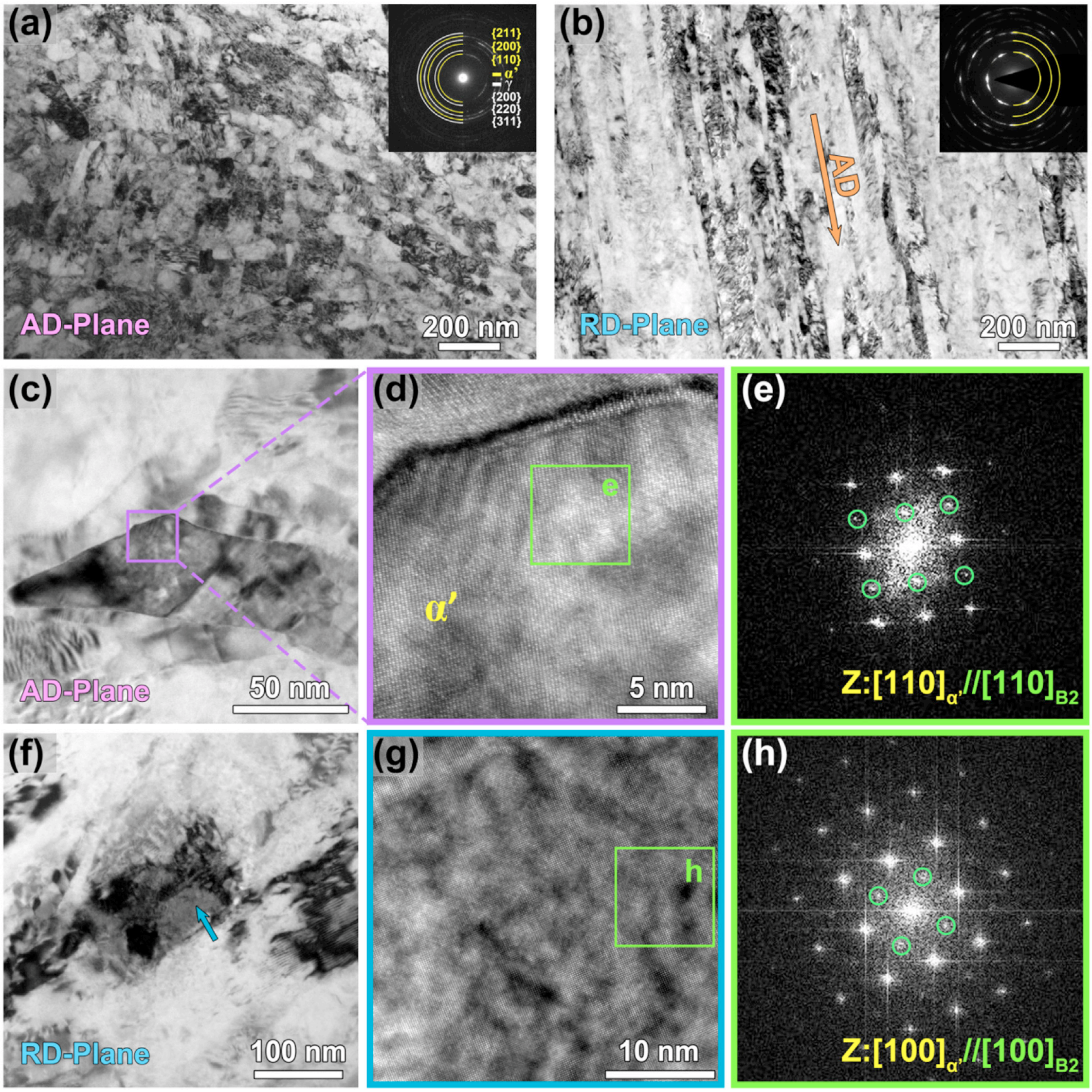

Fig. 10. Microstructures of the RS-450 sample. Low magnification bright-field TEM images showing typical microstructures observed on the (a) AD-plane and (b) RD-plane; insets are the corresponding SAED patterns. High magnification TEM images showing deformed sub-grains observed on the (c) AD-plane and (f) RD-plane; (d) HR-TEM image taken from the boxed area in (c); (e) FFT pattern deduced from the green-boxed area in (d). (g) HR-TEM image taken from the area marked by the blue arrowhead in (f). (h) FFT pattern deduced from the green-boxed area in (g).

in the RS-450 sample are shown. The boxed region in Fig. 10(c) is magnified in Fig. 10(d), which exhibits a BCT lattice structure oriented to the [81] zone axis. Fast Fourier transform (FFT) analysis performed on the boxed region in Fig. 10(d) yielded two sets of diffraction patterns shown in Fig. 10(e). The strong diffraction spots correspond to the α'-martensite on the [81] zone axis. The weak diffraction spots, indicated by green circles, correspond to the B2 phase on the [81] zone axis. Fig. 10(g) displays an atomic-resolution image of the area marked by the blue arrow in Fig. 10(f), showing the α'-martensite structure on the [82] zone axis. Again, the FFT image in Fig. 10(h) reveals the diffraction spots from the B2 phase that exhibit the sizes of only a few nanometers. The nano-sized B2 phase maintains a coincidence site lattice (CSL) relationship with the martensitic matrix: [81]B2 // [81]α' and [82]B2 // [82]α' [83]. Nano-sized B2 phases were randomly observed within the martensite grains of the RS-450 sample but were absent in the RS1.5 sample. Thus, the B2 phase forms via thermally induced phase transformation during the short-term annealing at 450 °C [20]. Unlike the B2 phase found in Al-containing lightweight steels, maraging steels, and medium-Mn steels [17–19], the nano-sized B2 phase in the RS-450 sample is electron beam sensitive and unstable. Under 300 kV electron beam scanning, the B2 phase quickly disappears, posing a challenge for STEM-EDS analysis. Additional attempts for characterizing the B2 phase in the 304 steels will be done by means of STEM with electrostatic dose modulator and lowered acceleration voltage, and atom probe tomography (APT), in our future work.

The RS-700 sample was made by annealing the RS1.5 sample at 700 °C for 10 min. As shown in Fig. 11(a), abnormal grain growth occurred, resulting in bundles of recrystallized ultrafine-grains (RX-UFGs) delineated by red dashed lines that grew larger than surrounding deformed sub-grains. As shown in Fig. 11(b), both deformed sub-grains and RX-UFGs are seen on the RD-plane, but they are mostly equiaxed and no longer elongated along the AD. Dislocations, nano-ATs and stacking faults (SFs) [16] can be found in the nanostructured austenite, as shown in Fig. 11(a) and (c). As revealed in Fig. 11(d), some nano-precipitates (the blurred light contrast spots) are found within the recrystallized austenite grains. In Fig. 11(e), the HR-TEM image and the corresponding FFT inset confirm that these precipitates are $M_{23}C_6$ carbides exhibiting

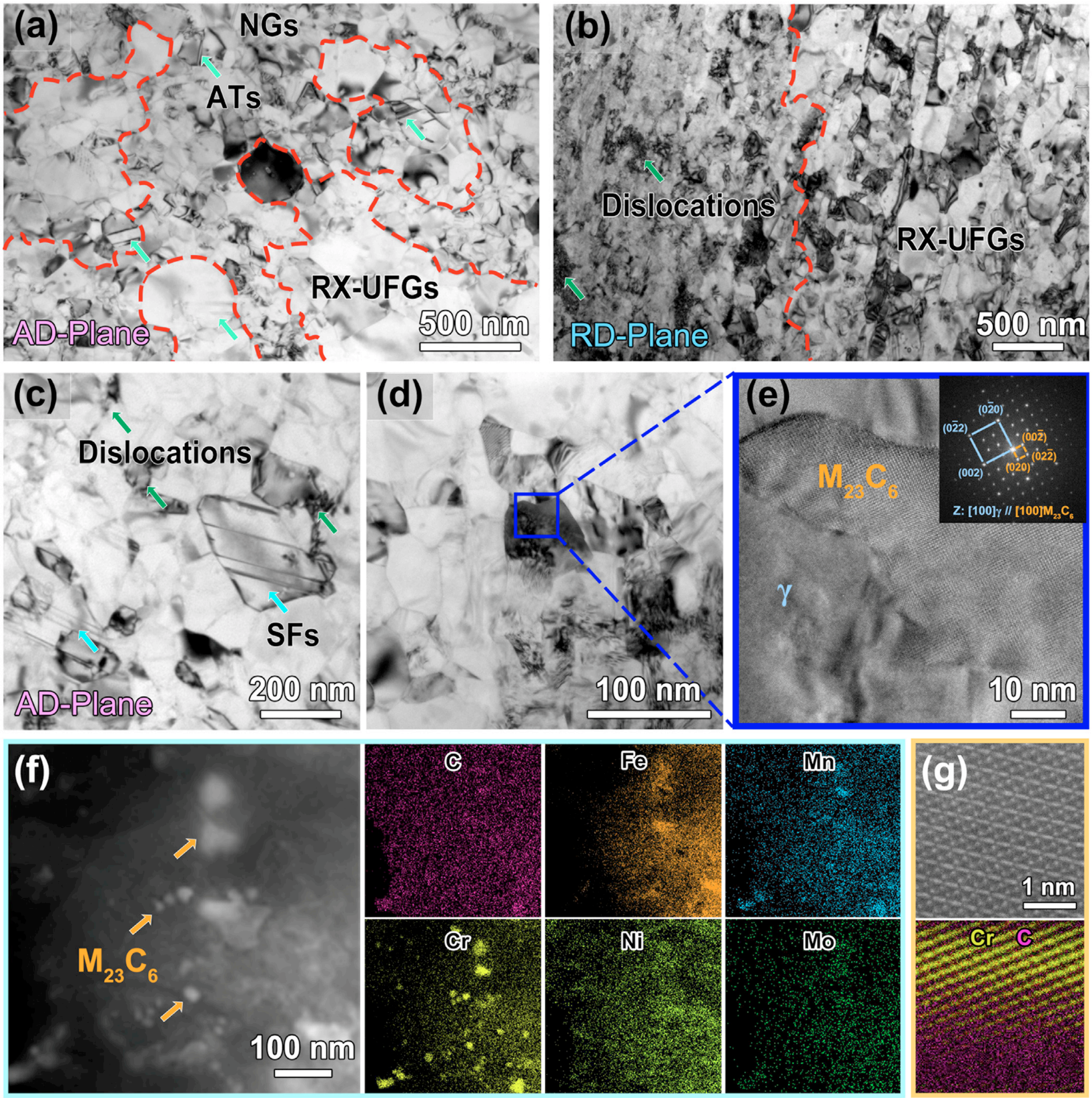

Fig. 11. Microstructures of the RS-700 sample. (a, b) Low-magnification bright-field TEM images showing microstructures on the (a) AD-plane and (b) RD-plane, respectively. (c) TEM image revealing dislocations and SFs. (d) TEM image presenting the morphology of precipitates. (e) HR-TEM image showing atomic structures in the blue-boxed area in (d), and the inset SAED pattern showing the [82] $M_{23}C_6//[100]\gamma$ orientation relationship. (f) STEM and EDS images showing compositions for the carbides. (g) HR-STEM image displaying the atomic structure of $M_{23}C_6$ with an atomic-scale EDS elemental overlay.

$<100>\gamma//<100>M_{23}C_6$ orientation relationship with the matrix. In Fig. 11(f), STEM images reveal some $M_{23}C_6$ carbides of various sizes. The corresponding EDS maps in Fig. 11(f) indicate that the precipitates are predominantly Cr-rich. The atomic-scale EDS map in Fig. 11(g) verifies that the carbides are Cr-rich $M_{23}C_6$.

Fig. 12(a) shows the microstructure in the RS-700 sample tensile deformed to fracture. The grain boundaries became ill-defined due to pronounced dislocation-boundary interactions. The inserted diffraction pattern shows bright diffraction rings for martensite but very dull rings for austenite. A high magnification TEM image in Fig. 12(b) shows a high density of dislocations inside a martensite grain. The inserted diffraction pattern shows only diffraction spots for martensite, and no diffraction spots for B2 phase at all.

4. Discussion

4.1. Source of ultra-high yield strength after RS

As shown in Fig. 4 and Table 2, rotary swaging processing has been very effective in strengthening the commercial 304 SS. In the current case, the yield strength of 304 SS continues to increase with increasing strain, and reaches 2235 MPa at the RS strain of

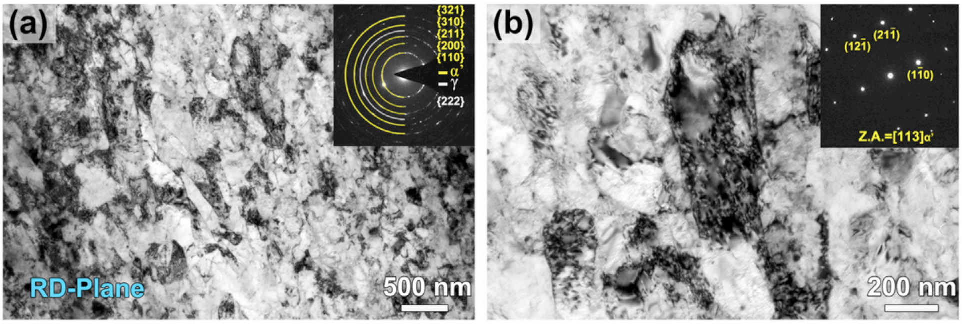

Fig. 12. TEM images showing microstructures in the RS-700 sample deformed to tensile fracture, at (a) low magnification and (b) high magnification.

1.5. Detailed microstructural characterization as shown in Figs. 5(b, c) and 9, reveals that the substantial increase in yield strength is attributed to a significant increase in dislocation density, extreme grain refinement and martensitic transformation in large volume fractions. As shown in Fig. 5(c), the dislocation densities in austenite and martensite of the RS1.5 sample are 2.42×10^{15} and 2.02×10^{15} m^{-2}, respectively. The average grain size (austenite and martensite mixed) is ~80 ± 51 nm (Fig. 9(c)); the volume fraction of martensite is ~68 % (Fig. 5(b)). According to literature, similar microstructural parameters can also be attained via cold rolling [84], ECAP [26] and HPT [85,86], but with a strain input much higher than 1.5.

The apparent microstructural change to the commercial 304 SS done by RS has to be explained from two perspectives, the processing route and the material. In terms of the processing route, as shown in Fig. 2(c), the RS process imposes multi-directional strains in radial and axial directions, and high strain rates in the radial directions, resulting in complex stress states in the 304 SS rod sample. Multi-directional strains are helpful for stimulating dislocations, twins and martensitic transformation in multiple slip systems. High strain rate can stimulate high flow stress, which in turn increases dislocation density [87], twin density [88], and volume fraction of martensite [89]. In terms of materials, 304 grade steels have very low SFE (14–36 mJ/m^2) [90], thus making them prone to deformation twinning and martensitic transformation during all sorts of cold working. Meanwhile, cross-slip, dynamic recovery and recrystallisation are difficult in 304 SS, because the dislocations tend to dissociate into partial dislocation pairs for planar slip rather than cross-slip [9]. To sum up, (1) RS imposes multi-directional strains to 304 SS with the low SFE, resulting in deformation twinning and martensitic transformation in multiple slip systems to subdivide the grains into domains with sizes of hundreds of nanometers, as shown in Fig. 9(a1); (2) High strain rates and low SFE help to reduce the thicknesses of deformation twins and martensite lamellae, as shown in Fig. 9(c2); (3) High strains and multi-directional strains can drastically increase the dislocation density, and meanwhile the low SFE delays dynamic recovery and recrystallisation to help sustain the high dislocation density and small grain size (the blurred and irregular sub-grain boundaries seen in Fig. 9(c1) suggest high dislocation densities and retarded dynamic recrystallisation).

It is known that both twin and phase boundaries are effective in blocking dislocation slip. Once deformation twins formed, the twin boundaries can trap dislocations and gradually develop into conventional high-angle grain boundaries [14]. Deformation twins are unstable and will mostly transform into martensite due to the low SFE of 304 SS and under the high flow stresses imposed by RS. The martensite phase boundaries can also trap dislocations under plastic deformation and change the orientation with respect to the adjacent grain, which can either be an austenite grain or martensite grain [91]. Therefore, the resultant ultrafine grains and nanograins inherit from the deformation twins and martensite, and the final grain sizes are comparable to the thicknesses of the deformation twins and martensite.

According to the microstructural characterization results in Figs. 5 and 9(c), it is apparent that grain boundary strengthening, dislocation strengthening and some other strengthening effects [92] (due to strain partitioning between soft and hard microstructures) contribute additively to the high yield strength of the RS1.5 sample. Therefore, the yield strength of the steel sample can be estimated by Eq. (2):

$$\sigma_y = \sigma_0 + \Delta\sigma_{\text{HP}} + \Delta\sigma_{\text{d}} + \Delta\sigma_{\text{other}} \tag{2}$$

where σ_0 is the lattice friction stress; $\Delta\sigma_{\text{HP}}$ and $\Delta\sigma_{\text{d}}$ are the strength increments due to boundary strengthening and dislocation strengthening, respectively; and $\Delta\sigma_{\text{other}}$ represents the combined strengthening contribution arising from the observed microstructural heterogeneities, predominantly encompassing: (i) α'-γ phase boundaries, (ii) nano-precipitates, and (iii) the boundaries between the hard deformed grains and soft recrystallized grains.

The empirical Hall-Petch equation is often used to estimate the strength increment due to grain boundary strengthening in polycrystalline alloys [93]:

$$\Delta\sigma_{\text{HP}} = k \cdot d^{-1/2} \tag{3}$$

where k is the Hall-Petch coefficient [94], and d is the average grain size.

The Bailey-Hirsch equation can be used to estimate the strength increment due to dislocation strengthening [95]:

$$\Delta\sigma_{\text{d}} = M\alpha G b\sqrt{\rho} \tag{4}$$

where M, α, G, b and ρ are, respectively, the Taylor factor (mean orientation factor), α is a temperature-dependent constant, G is the shear modulus, and b is the Burgers vector [94].

The parameters necessary for estimating the strength increments are collected in Table 3. The parameters d, M and ρ are estimated based on TEM, EBSD [96], and XRD [41] results, respectively. The texture at the *meso* scale [97,98], and the Schmid factor, local shear stress and the number of active slip systems at the micro scale [97], together determine the mean orientation factor M. In all three samples, the martensite phase (α') exhibits significantly higher M values than the austenite phase (γ) (Table 3). The austenite in RS1.5 sample has the lowest M. The M values for the austenite in RS-450 and RS-700 samples are 3.22 and 3.17, respectively. This is because the austenite was transformed from the martensite and also inherited the hard orientations. The RS-450 sample shows higher M values than the RS-700 sample, suggesting that annealing at 700 °C can drive the grains towards the soft orientations. The large M values for the martensite in RS1.5 and RS-450 samples signify substantial yield strength anisotropy at both macro and micro scales. The RS-700 sample contains predominantly austenite ($M(\gamma) = 3.17$); therefore, the large fraction of austenite with soft orientations substantially lowered the

Table 3
Parameters used for strength estimation.

Sample	Phase	σ_0 (MPa)	k (MPa μm$^{1/2}$)	d (nm)	M	α	G (GPa)	b (nm)	ρ (m^{-2})
RS1.5	Austenite	200.0 [94]	325 [94]	80	2.95	0.24 [99]	80 [99]	0.260 [94]	2.42×10^{15}
	Martensite	82.5 [100]	390 [100]	80	3.47	0.25 [82]	80 [82]	0.248 [82]	2.02×10^{15}
RS-450	Austenite	200.0	325	88	3.22	0.24	80	0.260	1.04×10^{15}
	Martensite	82.5	390	88	3.44	0.25	80	0.248	1.66×10^{15}
RS-700	Austenite	200.0	325	206	3.17	0.24	80	0.260	1.74×10^{14}
	Martensite	82.5	390	169	3.33	0.25	80	0.248	1.22×10^{14}

Table 4
Empirical calculation results of strength increments (MPa).

Sample	$\Delta\sigma_{HP}$	$\Delta\sigma_d$	σ_0	$\Delta\sigma_{other}$	σ_y
RS1.5	1305.32	761.51	120.10	48.07	2235
RS-450	1268.68	661.72	107.18	337.43	2375
RS-700	736.53	206.56	189.66	157.25	1290

strength of the steel. The texture effect contributes to $\Delta\sigma_d$ in Eq. (4). The rest of the parameters are adopted from the literature [82,94,99,100]. $\Delta\sigma_{HP} =$ 1305.32 MPa and $\Delta\sigma_d =$ 761.51 MPa are estimated by using Eqs. (3) and (4), and the rule of mixture. For simplicity, the strengthening effects attributed to the complex microstructural heterogeneities consisting of α'-γ phase boundaries, B2 nano-precipitates, $M_{23}C_6$ carbides, hard deformed grains and soft recrystallized grains, are consolidated to a single parameter $\Delta\sigma_{other}$. The value of $\Delta\sigma_{other}$ for RS1.5 (48.07 MPa) was deduced by substituting the experimentally measured yield strength into Eq. (2). The strength increments calculated for all samples are summarized in Table 4.

4.2. Record high yield strength attained in the RS-450 sample

The record high yield strength of 2375 MPa has been successfully obtained for the RS-450 sample, surpassing all known 304 steels processed by different methods and even many high-strength steels, as shown in Fig. 4(a). Considering that the RS-450 sample is obtained by annealing the RS1.5 sample at 450 °C for 10 min, the short-time annealing has increased the yield strength by ~140 MPa. Annealing strengthening has been reported in some plastically deformed alloys [101–104], and is explained by the reduction of dislocation sources [16], free energy reduction by cell formation [101], solute segregation to defects [102], and precipitation [20]. In the current case, the dislocation density in the RS-450 sample is only slightly lower than the RS1.5 sample, but still at a high-level of 10^{15} m^{-2}, as shown in Fig. 5(c) and Table 3. Therefore, the effect of dislocation source reduction can be considered negligible. The statistically averaged grain size of ~88 ± 60 nm in the RS-450 sample is estimated from TEM images, in which dislocation boundaries and grain boundaries are hardly distinguishable. It is very common for TEM and XRD analysis to mistake cell walls as grain boundaries [105]. Therefore, if a significant number of dislocation cells were formed, the average grain size should be reduced rather than increased. Provided that the measured average grain sizes show relatively large standard deviations (80 ± 51 nm for RS1.5 and 88 ± 60 nm for RS-450), the change in average grain size from 80 nm to 88 nm seems negligible. While cell formation due to recovery cannot be ruled out, the negligible change in average grain size after short-time annealing could be a combined result of recovery and grain growth. 304 steels are rich in alloying contents, meanwhile, the high density of lattice defects induced by RS can change the segregation and precipitation kinetics upon annealing [14]. Therefore, elemental segregation to defects such as dislocations and grain boundaries is very likely, but the resultant strength increment is very difficult to quantify in such a complex alloy system. Considering that the annealing temperature is comparatively low and the annealing time is short, short-range reshuffling of the constituents is more likely than long-range diffusion [20]. Therefore, the direct effect of elemental segregation on strength is considered small. As shown in Fig. 10(e) and (h), nano-sized B2 precipitates are identified inside the ultrafine martensite grains. In recent years, the strengthening effect of B2 nano-precipitates in steels and high entropy alloys has received much attention [17,19,20,106,107]. In Ni and/or Al rich high alloy steels, Ni(Al,Fe) nano-precipitates with a B2 structure usually form upon annealing at ~500 °C [20]. The B2 nano-precipitates are highly coherent with the BCC/BCT martensite matrix. The low lattice misfit between nano-precipitates and matrix decreases the nucleation barrier for precipitation, thus enabling and stabilizing nano-precipitates with a large number density at the interior of martensite grains. The in-depth research work by Jiang et al. [20] proves that the small elastic misfit strains around the B2 nano-precipitates contribute marginally to dislocation interactions/strengthening. Instead, it is the local chemical ordering and modulus mismatch contributing to the precipitation strengthening effect.

In addition to the above-mentioned strengthening mechanisms, annealing-induced martensitic transformation is unignorable and crucial, because, as shown in Fig. 5(b), the volume fraction of martensite is increased by 11 % to 79 %. Martensitic transformation in metastable austenitic steels due to short-time annealing in the temperatures 330–450 °C, may be governed by three mechanisms: (1) the precipitation of carbides which locally increases the martensitic transformation temperature (M_s) and so promotes additional α' formation during the cooling stage of the annealing treatment [81,108]; (2) thermal nucleation of new martensite particles which shall have the characteristic lenticular appearance [109]; (3) the growth of existing α' laths due to relaxation of α'-γ interfaces as a part of the recovery process [108]. Fig. 10 shows typical microstructures in the RS-450 sample, and there is no trace of lenticular martensite at all. Therefore, nucleation of new martensite particles is ruled out in the present study. The RS-450 sample has undergone large strain deformation under tensile stress in the axial direction and compressive stress in the radial directions prior to annealing, and thus, many of the α'-γ interfaces possess high energies and are under compressive stresses. Therefore, moderate thermal input may trigger expansions of α' laths via recovery of partial dislocations at α'-γ interfaces, permitting relaxation of the local compressive stresses [108].

After systematic analysis and discussion, it is concluded that the annealing-induced strengthening in the RS-450 sample is mainly attributed to the formation of B2 nano-precipitates and increased volume fraction of α' martensite, offsetting the effect of recovery. According to the empirical calculation results given in Table 4, the contributions from grain boundary strengthening ($\Delta\sigma_{HP} =$ 1268.68 MPa) and dislocation strengthening ($\Delta\sigma_d =$ 661.72 MPa) for the RS-450 are smaller than for the RS1.5 sam-

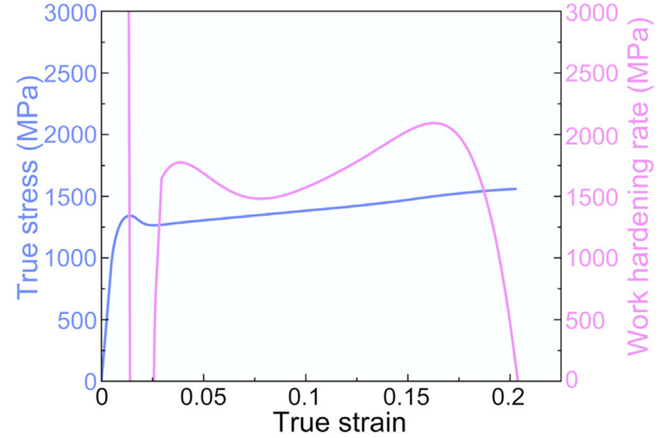

Fig. 13. True stress-strain and work hardening rate curves for the RS-700 sample.

ple, primarily due to recovery. However, the strength increment ($\Delta\sigma_{\text{other}}$ = 337.43 MPa) attributed to precipitates and α'-γ interfaces for the RS-450 is significantly larger than that of the RS1.5 sample. In summary, the B2 nano-precipitates within the α' martensite together are a potent strengthening feature that significantly elevates the yield strength of the 304 SS to a new record level.

4.3. Mechanical properties and synergistic deformation mechanisms in the RS-700 sample

As shown in Fig. 4(c) and (d), the RS-700 sample possesses an excellent combination of strength and ductility, which are attributed to the synergistic deformation mechanisms involving martensitic transformation, deformation twinning, dislocation activities, and precipitates-related mechanisms. As shown in Fig. 5(b) and (c), annealing the RS1.5 sample at 700 °C for 10 min has drastically reduced both the fraction of martensite and total dislocation density to 8.8 % and 1.82 × 10^{14} m^{-2}, respectively. As shown in Figs. 7 and 11, the remnant martensite is ultrafine/nano grains dispersed among the ultrafine austenite grains. $M_{23}C_6$ (M is mainly Cr) carbides exhibiting semi-coherent and/or incoherent interfaces with the austenite matrix have been reported [110–112]. The $M_{23}C_6$ carbides larger than a critical size of ~50–100 nm, as shown in Fig. 11(e) and (f), can effectively strengthen the steel via the Orowan bypass mechanism [113]. Given that the RS-700 sample exhibits a yield strength of 1290 MPa, the contribution of $M_{23}C_6$ carbides is significant, enhancing strength by impeding dislocation glide.

The RS-700 sample exhibits excellent strength, ductility, and strain hardening at room temperature. This is primarily attributed to the martensitic transformation-induced plasticity (TRIP) effect. The SFE is one of the decisive factors influencing the deformation mechanisms. For metallic materials, an SFE below 20 $\mathrm{mJ/m^2}$ favors deformation-induced martensitic transformation; an SFE ranging from 20 to 45 $\mathrm{mJ/m^2}$ promotes deformation twinning; whereas an SFE exceeding 45 $\mathrm{mJ/m^2}$ favors dislocation slip as the primary deformation mechanism [114]. The SFE of an austenitic stainless steel at room temperature can be estimated by [90]:

$$\gamma_{\text{SFE}}\left(\mathrm{mJ/m^2}\right) = -53+6.2(\%\mathrm{Ni})+0.7(\%\mathrm{Cr})+3.2(\%\mathrm{Mn}) +9.3(\%\mathrm{Mo}) \qquad (5)$$

The SFE of the 304 SS investigated in this work is estimated by Eq. (5) as 14.2 $\mathrm{mJ/m^2}$, which is sufficiently low to promote martensitic transformation. Fig. 13 presents the true stress-strain curves and work hardening rate ($\mathrm{d}\sigma/\mathrm{d}\varepsilon$) curves for the RS-700 sample. Yield drop occurred in the early stage of plastic deformation, corresponding to the sharp drop and rise of the work hardening rate curve. This is attributed to the initiation of Lüders-type deformation in UFG austenitic stainless steel [115]. The work hardening rate curve can be divided into two distinct stages. In the first stage (true strain range of 0.04–0.08, Fig. 13), the volume fraction of martensite increases rapidly, but the dislocation density hardly changes, as shown in Fig. 6. Apparently, martensitic transformation carries the plastic strain, but provides a trivial hardening effect. At a true strain of 0.08, the volume fraction of martensite reached 49 % and increased slowly beyond. Meanwhile, the dislocation densities in both austenite and martensite begin to rise simultaneously to increase the work hardening rate.

To further analyze the tensile behavior under the TRIP effect, DIC was employed to quantify full-field strain evolution. As shown in Fig. 6(b), the tensile stress of the RS-700 sample first reached a peak value of 1323.8 MPa at a strain of 0.7 %, then quickly dropped to 1230.8 MPa at a strain of 2 %. Meanwhile, a blue band of strain concentration formed, as shown in the 2 % DIC contour map. As the tensile deformation proceeds, from 2 % to 20 % strain, the stress-strain curve develops a plateau, and correspondingly the strain band expands gradually to cover the entire tensile specimen, demonstrating the Lüders-like deformation which is due to the dynamic balance between strain localization and martensitic transformation induced hardening [115–117]. According to the empirical calculation results provided in Table 4, $\Delta\sigma_{\text{other}}$ = 157.25 MPa is smaller than that of the RS-450 sample, indicating that the precipitation and interfacial strengthening effects in the RS-700 are moderate. Meanwhile, at the early stage of deformation, when the strain is smaller than 8 %, the dislocation density in austenite is only marginally higher than that in martensite, and the dislocation densities increase slowly. However, the volume fraction of martensite increased dramatically to 49.0 %. Therefore, the plastic deformation at the early stage is dominated by martensitic transformation, which competes against dislocation accumulation [118]. This is because the α'-γ interfaces are mostly unstable, instead of accumulating or interacting with dislocations, the interfaces shear across the austenite grains to accommodate the plastic strains. Once a sufficiently large number of stable α'-γ interfaces formed after 8 % of tensile strain, dislocations began to accumulate at a fast rate, indicated by the increased slope of dislocation density curve of austenite, as shown in Fig. 6(b). Figs. 8 and 12 show the microstructure at the fracture tip of the RS-700 sample, where the volume fraction of martensite is close to 100 %. As shown in Fig. 12(b), the martensite grain contains many dislocation debris, but neither B2 nor $M_{23}C_6$ carbide nano-precipitate is found inside the grain. Apparently, martensitic transformation has wiped out $M_{23}C_6$ carbides when shearing across the austenite grains. B2 precipitates did not form under room temperature plastic deformation.

5. Conclusions

Via industrial RS and annealing treatment, the microstructure and mechanical properties of a commercial 304 SS can be modified in wide ranges. Three major conclusions are drawn below:

(1) The equivalent strain of 1.5 imposed by RS is capable of processing the 304 SS to the ultra-high strength of 2220 MPa. The RS1.5 sample has an average grain size of ~80 nm, volume fraction of martensite of ~68 % and total dislocation density of ~2.15 × 10^{15} m^{-2}. Apparently, the ultra-high YS is attributed to extreme grain refinement, conspicuous martensitic transformation and dislocation accumulation.

(2) Subsequent annealing treatment at 450 °C for 10 min to the RS1.5 sample further increased the YS to a record high of

2360 MPa. The short-time annealing increased the volume fraction of nanostructured martensite to 79 % via the growth of existing α' laths due to relaxation of α'-γ interfaces. The extremely high strength of the RS-450 sample is thus attributed to the large fraction of martensite and B2 nano-precipitates.

(3) Subsequent annealing treatment at 700 °C for 10 min to the RS1.5 sample drastically reduced the fraction of martensite, resulting in the heterostructure consisting of remnant ultrafine martensite, nano-sized $M_{23}C_6$ carbides and a small fraction of coarse-grained austenite. The RS-700 sample demonstrates Lüders-like tensile deformation due to the dynamic balance between strain localization and martensitic transformation induced hardening, and thus shows an excellent combination of 1320 MPa YS and 20.5 % UE.

Declaration of competing interest

The authors declare that they have no known competing financial interests or personal relationships that could have appeared to influence the work reported in this paper.

CRediT authorship contribution statement

Weiheng Xia: Writing – original draft, Investigation, Formal analysis, Data curation, Conceptualization. **Jiaqi Meng:** Investigation, Data curation. **Runchang Liu:** Formal analysis. **Zongyao Li:** Investigation. **Yang Cao:** Writing – review & editing, Supervision. **Yonghao Zhao:** Supervision, Funding acquisition, Conceptualization.

Acknowledgements

This work was financially supported by the National Key R&D Program of China (2021YFA1200203), the National Natural Science Foundation of China (51971112, 51225102, and 52071181), the Six Talent Peaks Project of Jiangsu Province (2017-XCL-051), and Jiangsu Province Leading Edge Technology Basic Research Major Project (BK20222014). This work was supported by the Materials Characterization Facility of Nanjing University of Science and Technology, the Centre for High-Resolution Electron Microscopy (CħEM), ShanghaiTech University (EM02161943) and Shanghai Key Laboratory of High-resolution Electron Microscopy, Shanghai Science and Technology Plan. The authors thank Prof. Qing Zhang from ShanghaiTech University and Lingling Wang from JEOL (BEIJING) Co., Ltd. Shanghai Branch for the technical support.

References

[1] N. Li, S. Shi, J. Luo, J. Lu, N. Wang, Surf. Coat. Technol. 309 (2017) 227–231.
[2] A.Y. Chen, L.L. Zhu, L.G. Sun, J.B. Liu, H.T. Wang, X.Y. Wang, J.H. Yang, J. Lu, Nat. Commun. 10 (2019) 1403.
[3] P.M. Ahmedabadi, V. Kain, K. Venkata Muralidhar, I. Samajdar, J. Nucl. Mater. 432 (2013) 243–251.
[4] Y.-L. Song, C.-S. Li, B.-Z. Li, Y.-H. Han, Mater. Sci. Eng. A 742 (2019) 662–671.
[5] R.K. Gupta, N. Birbilis, Corros. Sci. 92 (2015) 1–15.
[6] J. Liu, C. Chen, Q. Feng, X. Fang, H. Wang, F. Liu, J. Lu, D. Raabe, Mater. Sci. Eng. A 703 (2017) 236–243.
[7] R.K.C. Nkhoma, C.W. Siyasiya, W.E. Stumpf, J. Alloy. Compd. 595 (2014) 103–112.
[8] A. Zarei, M. Akbari, A. Abdollahi, H. Soleimanimehr, Heliyon 10 (2024) e39954.
[9] J. Lu, L. Hultman, E. Holmström, K.H. Antonsson, M. Grehk, W. Li, L. Vitos, A. Golpayegani, Acta Mater. 111 (2016) 39–46.
[10] D.P. Braga, L.M. Corrêa, V.L. Sordi, C.A. Della Rovere, O.M. Cintho, A.M. Kliauga, Mater. Sci. Eng. A 863 (2023) 144527.
[11] Z. Wang, S. Shi, J. Yu, B. Li, Y. Li, X. Chen, Scr. Mater. 234 (2023) 115581.
[12] H.E. Sabzi, E. Hernandez-Nava, X.-H. Li, H. Fu, D. San-Martín, P.E.J. Rivera-Díaz-del-Castillo, Mater. Des. 212 (2021) 110246.
[13] A. Zargaran, T.T.T. Trang, G. Park, N.J. Kim, Acta Mater. 220 (2021) 117349.
[14] Y. Cao, S. Ni, X. Liao, M. Song, Y. Zhu, Mater. Sci. Eng. R 133 (2018) 1–59.
[15] Z. Zhou, S. Wang, J. Li, Nano Mater. Sci. 2 (2020) 80–82.
[16] M. Liu, W. Gong, R. Zheng, J. Li, Z. Zhang, S. Gao, C. Ma, N. Tsuji, Acta Mater. 226 (2022) 117629.
[17] J.-Y. Kim, J.-S. Kim, T. Song, J.-K. Kim, J. Mater. Res. Technol. 27 (2023) 905–919.
[18] F. Guo, M. Wang, P. Ye, Y. Zhai, C. Zhang, Q. Cheng, W. Su, Q. Wang, J. Liang, W. Cao, C. Huang, Mater. Sci. Eng. A 890 (2024) 145886.
[19] S.-H. Kim, H. Kim, N.J. Kim, Nature 518 (2015) 77–79.
[20] S. Jiang, H. Wang, Y. Wu, X. Liu, H. Chen, M. Yao, B. Gault, D. Ponge, D. Raabe, A. Hirata, M. Chen, Y. Wang, Z. Lu, Nature 544 (2017) 460–464.
[21] X. Wu, M. Yang, F. Yuan, G. Wu, Y. Wei, X. Huang, Y. Zhu, Proc. Natl. Acad. Sci. 112 (2015) 14501–14505.
[22] Y. Zhu, X. Wu, Prog. Mater. Sci. 131 (2023) 101019.
[23] J. Hu, X. Li, Z. Zhang, L. Wang, Y. Li, W. Xu, Mater. Res. Lett. 11 (2023) 648–654.
[24] L. Romero-Resendiz, M. El-Tahawy, T. Zhang, M.C. Rossi, D.M. Marulanda-Cardona, T. Yang, V. Amigó-Borrás, Y. Huang, H. Mirzadeh, I.J. Beyerlein, J.C. Huang, T.G. Langdon, Y.T. Zhu, Mater. Sci. Eng. R 150 (2022) 100691.
[25] R.Z. Valiev, I.V. Alexandrov, Nanostruct. Mater. 12 (1999) 35–40.
[26] K. Hajizadeh, K.J. Kurzydlowski, Mater. Today Commun. 35 (2023) 105641.
[27] K. Kishore, R.G. Kumar, A.K. Chandan, Mater. Sci. Eng. A 803 (2021) 140675.
[28] Q. Mao, Y. Liu, Y. Zhao, J. Alloy. Compd. 896 (2022) 163122.
[29] Y. Liu, J. Ren, S. Guan, C. Li, Y. Zhang, S. Muskeri, Z. Liu, D. Yu, Y. Chen, K. An, Y. Cao, W. Liu, Y. Zhu, W. Chen, S. Mukherjee, T. Zhu, W. Chen, Acta Mater. 250 (2023) 118884.
[30] A. Meng, X. Chen, J. Nie, L. Gu, Q. Mao, Y. Zhao, J. Alloy. Compd. 859 (2021) 158222.
[31] X. Chen, C. Liu, Y. Wan, S. Jiang, Z. Chen, Y. Zhao, Metall. Mater. Trans. A 52 (2021) 4053–4065.
[32] Y. Wan, B. Tang, Y. Gao, L. Tang, G. Sha, B. Zhang, N. Liang, C. Liu, S. Jiang, Z. Chen, X. Guo, Y. Zhao, Acta Mater. 200 (2020) 274–286.
[33] Y. Yang, X. Chen, J. Nie, K. Wei, Q. Mao, F. Lu, Y. Zhao, Mater. Res. Lett. 9 (2021) 255–262.
[34] Q. Mao, L. Wang, J. Nie, Y. Zhao, Compos. Part B-Eng. 231 (2022) 109567.
[35] Q. Mao, Y. Zhang, J. Liu, Y. Zhao, Nano Lett. 21 (2021) 3191–3197.
[36] Q. Mao, Y. Zhang, Y. Guo, Y. Zhao, Commun. Mater. 2 (2021) 46.
[37] J. Nie, F. Lu, Z. Huang, X. Ma, H. Zhou, C. Chen, X. Chen, H. Yang, Y. Cao, X. Liu, Y. Zhao, Y. Zhu, Materialia 9 (2020) 100523.
[38] Y. Yang, J. Nie, Q. Mao, Y. Zhao, Results Phys. 13 (2019) 102236.
[39] F. Lu, J. Nie, X. Ma, Y. Li, Z. Jiang, Y. Zhang, Y. Zhao, X. Liu, Mater. Sci. Eng. A 770 (2020) 138519.
[40] C. Hu, C. He, X. Zhu, H. Dong, X. Wan, G. Li, K. Wu, Mater. Sci. Eng. A 887 (2023) 145748.
[41] A.K. De, D.C. Murdock, M.C. Mataya, J.G. Speer, D.K. Matlock, Scr. Mater. 50 (2004) 1445–1449.
[42] A. Hedayati, A. Najafizadeh, A. Kermanpur, F. Forouzan, J. Mater. Process. Technol. 210 (2010) 1017–1022.
[43] R. Singh, D. Sachan, R. Verma, S. Goel, R. Jayaganthan, A. Kumar, Mater. Today Proc. 5 (2018) 16880–16886.
[44] S. Sunil, R. Kapoor, S.K. Sarkar, A.Biswas Sarita, H. Donthula, D. Sen, Acta Mater. 221 (2021) 117379.
[45] Q. Pan, L. Zhang, R. Feng, Q. Lu, K. An, A.C. Chuang, J.D. Poplawsky, P.K. Liaw, L. Lu, Science 374 (2021) 984–989.
[46] Y.T. Sun, X. Kong, Z.B. Wang, Int. J. Plast. 155 (2022) 103336.
[47] R. Singh, D. Singh, D. Sachan, S.D. Yadav, A. Kumar, J. Mater. Eng. Perform. 30 (2021) 290–301.
[48] Y. Mine, K. Koga, K. Takashima, Z. Horita, Mater. Sci. Eng. A 661 (2016) 87–95.
[49] S.S. Satheesh Kumar, M. Vasanth, V. Singh, P. Ghosal, T. Raghu, J. Alloy. Compd. 699 (2017) 1036–1048.
[50] J. Sun, X. Wang, J. Li, D. Shu, S. Wang, P. Peng, Q. Mao, T. Liu, X. Lu, Y. Li, D. Zhu, G. Wang, W. Qin, Vacuum 187 (2021) 110116.
[51] Z. Wang, S. Shi, J. Yu, B. Li, Y. Li, X. Chen, Scr. Mater. 222 (2023) 115024.
[52] Z.J. Zheng, J.W. Liu, Y. Gao, Mater. Sci. Eng. A 680 (2017) 426–432.
[53] C. Ye, A. Telang, A.S. Gill, S. Suslov, Y. Idell, K. Zweiacker, J.M.K. Wiezorek, Z. Zhou, D. Qian, S.R. Mannava, V.K. Vasudevan, Mater. Sci. Eng. A 613 (2014) 274–288.
[54] Y. Mine, N. Horita, Z. Horita, K. Takashima, Int. J. Hydrog. Energy 42 (2017) 15415–15425.
[55] F.Javadzadeh Kalahroudi, H. Koohdar, T.G. Langdon, M. Nili-Ahmadabadi, Mater. Sci. Eng. A 804 (2021) 140519.
[56] Y. Mine, D. Haraguchi, Z. Horita, K. Takashima, Philos. Mag. Lett. 95 (2015) 269–276.
[57] H. Wang, I. Shuro, M. Umemoto, K. Ho-Hung, Y. Todaka, Mater. Sci. Eng. A 556 (2012) 906–910.
[58] G. Jang, J.N. Kim, H. Lee, T. Lee, N. Enikeev, M. Abramova, R.Z. Valiev, H.S. Kim, C.S. Lee, Mater. Sci. Eng. A 827 (2021) 142073.
[59] S.V. Dobatkin, O.V. Rybalchenko, N.A. Enikeev, A.A. Tokar, M.M. Abramova, Mater. Lett. 166 (2016) 276–279.
[60] J.Y. Kang, J.G. Kim, S.K. Kim, K.-G. Chin, S. Lee, H.S. Kim, Scr. Mater. 123 (2016) 122–125.
[61] J.G. Kim, Materialia 13 (2020) 100837.
[62] M.M. Abramova, N.A. Enikeev, R.Z. Valiev, A. Etienne, B. Radiguet, Y. Ivanisenko, X. Sauvage, Mater. Lett. 136 (2014) 349–352.
[63] H. Ueno, K. Kakihata, Y. Kaneko, S. Hashimoto, A. Vinogradov, Acta Mater. 59 (2011) 7060–7069.
[64] C.X. Huang, G. Yang, Y.L. Gao, S.D. Wu, Z.F. Zhang, Mater. Sci. Eng. A 485 (2008) 643–650.

[65] B.J. Kim, M. Abramova, H.S. Kim, N. Enikeev, J.G. Kim, Mater. Lett. 349 (2023) 134841.
[66] C. Haase, O. Kremer, W. Hu, T. Ingendahl, R. Lapovok, D.A. Molodov, Acta Mater. 107 (2016) 239–253.
[67] S.V. Dobatkin, W. Skrotzki, O.V. Rybalchenko, V.F. Terent'ev, A.N. Belyakov, D.V. Prosvirnin, G.I. Raab, E.V. Zolotarev, Mater. Sci. Eng. A 723 (2018) 141–147.
[68] G. Sun, L. Du, J. Hu, B. Zhang, R.D.K. Misra, Mater. Sci. Eng. A 746 (2019) 341–355.
[69] G.S. Sun, L.X. Du, J. Hu, H. Xie, H.Y. Wu, R.D.K. Misra, Mater. Charact. 110 (2015) 228–235.
[70] Z. Liu, Y. Han, Z. Wu, J. Sun, G. Zu, W. Zhu, X. Ran, Mater. Today Commun. 33 (2022) 104860.
[71] H.A. Rezaei, M.S. Ghazani, B. Eghbali, Mater. Sci. Eng. A 736 (2018) 364–374.
[72] S. Mohammadzehi, M. Roostaei, H. Mirzadeh, R. Mahmudi, I. Weißensteiner, Mater. Charact. 214 (2024) 114072.
[73] P. Kusakin, A. Belyakov, C. Haase, R. Kaibyshev, D.A. Molodov, Mater. Sci. Eng. A 617 (2014) 52–60.
[74] L. Kubin, Science 312 (2006) 864–865.
[75] Y. Jiang, X. Zhou, X.Y. Li, K. Lu, Acta Mater. 256 (2023) 119134.
[76] X.-S. Yang, S. Sun, H.-H. Ruan, S.-Q. Shi, T.-Y. Zhang, Acta Mater. 136 (2017) 347–354.
[77] C.X. Huang, G. Yang, C. Wang, Z.F. Zhang, S.D. Wu, Metall. Mater. Trans. A 42 (2011) 2061–2071.
[78] Y. Zhu, X. Wu, Mater. Res. Lett. 7 (2019) 393–398.
[79] D.P. Yang, D. Wu, H.L. Yi, Scr. Mater. 161 (2019) 1–5.
[80] Q. Pan, S. Guo, F. Cui, L. Jing, L. Lu, Nanomaterials 11 (2021) 2613.
[81] S.S.M. Tavares, D. Fruchart, S. Miraglia, J. Alloy. Compd. 307 (2000) 311–317.
[82] C. Wang, Int. J. Plast. 150 (2022) 103191.
[83] G. Han, Z.J. Xie, B. Lei, W.Q. Liu, H.H. Zhu, Y. Yan, R.D.K. Misra, C.J. Shang, Mater. Sci. Eng. A 730 (2018) 119–136.
[84] T. Shintani, Y. Murata, Acta Mater. 59 (2011) 4314–4322.
[85] J.G. Li, M. Umemoto, Y. Todaka, K. Tsuchiya, Mater. Sci. Forum 561 (565) (2007) 847–852.
[86] M. El-Tahawy, Y. Huang, T. Um, H. Choe, J.L. Lábár, T.G. Langdon, J. Gubicza, J. Mater. Res. Technol. 6 (2017) 339–347.
[87] M. Qi, C. Chen, X. Li, N. Xiao, X. Mei, G. Su, F. Yang, X. Liu, Z. Guo, Mater. Sci. Eng. A 916 (2024) 147319.
[88] M. Wang, X.Y. Xu, H.Y. Wang, L.H. He, M.X. Huang, Acta Mater. 201 (2020) 102–113.
[89] Y. Yu, Y. Zhang, S. Xu, J. Han, J. Li, C. Guo, F. Jiang, G. Zhao, Z. Zhang, Int. J. Plast. 173 (2024) 103887.
[90] A.F. Padilha, R.L. Plaut, P.R. Rios, ISIJ Int. 43 (2003) 135–143 .
[91] B. Gao, Q. Lai, Y. Cao, R. Hu, L. Xiao, Z. Pan, N. Liang, Y. Li, G. Sha, M. Liu, H. Zhou, X. Wu, Y. Zhu, Sci. Adv. 6 (2020) eaba8169.
[92] X. Dong, B. Gao, L. Xiao, J. Hu, M. Xu, Z. Li, J. Meng, X. Han, H. Zhou, Y. Zhu, Adv. Funct. Mater. 34 (2024) 2410521.
[93] F. Otto, A. Dlouhý, Ch. Somsen, H. Bei, G. Eggeler, E.P. George, Acta Mater. 61 (2013) 5743–5755.
[94] S. Sunil, R. Kapoor, J.B. Singh, Mater. Charact. 205 (2023) 113353.
[95] S. Guan, Mater. Sci. Eng. A 761 (2019) 138056.
[96] W. Jiang, X. Guo, Y. Deng, Mater. Sci. Eng. A 858 (2022) 144155.
[97] M.J. Starink, S.C. Wang, Acta Mater. 51 (2003) 5131–5150.
[98] L.S. Toth, C.F. Gu, B. Beausir, J.J. Fundenberger, M. Hoffman, Acta Mater. 117 (2016) 35–42.
[99] M. Yang, L. Lei, Y. You, P. Wang, F. Xu, F. Zhao, Y. Liang, Mater. Des. 244 (2024) 113123.
[100] Z. Liu, Mater. Sci. Eng. A 787 (2020) 139529.
[101] Q. Cheng, X.D. Xu, P. Xie, L.L. Han, J.Y. He, X.Q. Li, J. Zhang, Z.T. Li, Y.P. Li, B. Liu, T.G. Nieh, M.W. Chen, J.H. Chen, J. Mater. Sci. Technol. 91 (2021) 270–277.
[102] C. Liu, X. Chen, D. Tolnai, Y. Hu, W. Zhang, Y. Zhang, F. Pan, J. Mater. Sci. Technol. 144 (2023) 70–80.
[103] O. Renk, A. Hohenwarter, V. Maier-Kiener, R. Pippan, J. Alloy. Compd. 935 (2023) 168005.
[104] S. Yuan, H. Fu, L. Qian, C.F. Cheung, X.-S. Yang, J. Mater. Sci. Technol. 170 (2024) 156–166.
[105] D.A. Hughes, N. Hansen, Acta Mater. 48 (2000) 2985–3004.
[106] B. Mishra, R. Sarkar, V. Singh, A. Mukhopadhyay, R.T. Mathew, V. Madhu, M.J.N.V. Prasad, Materialia 20 (2021) 101198.
[107] N. Yurchenko, E. Panina, A. Tojibaev, S. Zherebtsov, N. Stepanov, Mater. Res. Lett. 10 (2022) 813–823.
[108] K.B. Guy, E.P. Butler, D.R.F. West, Met. Sci. 17 (1983) 167–176.
[109] P.L. Mangonon, G. Thomas, Metall. Trans. 1 (1970) 1577–1586.
[110] M. Mitsuhara, S. Yamasaki, M. Miake, H. Nakashima, M. Nishida, J. Kusumoto, A. Kanaya, Philos. Mag. Lett. 96 (2016) 76–83.
[111] T. Hatakeyama, K. Sawada, Mater. Lett. 363 (2024) 136277.
[112] Y.Y. Song, X.Y. Li, L.J. Rong, D.H. Ping, F.X. Yin, Y.Y. Li, Mater. Lett. 64 (2010) 1411–1414.
[113] Q. Wang, D. Kong, X. Li, S. Zhou, Z. Zhang, Mater. Sci. Eng. A 919 (2025) 147504.
[114] S. Allain, J.-P. Chateau, O. Bouaziz, S. Migot, N. Guelton, Mater. Sci. Eng. A 387 (389) (2004) 158–162.
[115] S. Gao, Y. Bai, R. Zheng, Scr. Mater. 159 (2019) 28–32.
[116] X.G. Wang, Mater. Sci. Eng. A 674 (2016) 59–63.
[117] L. Fu, Z. Li, H. Wang, W. Wang, A. Shan, Scr. Mater. 67 (2012) 297–300.
[118] M.J. Sohrabi, H. Mirzadeh, C. Dehghanian, J. Mater. Eng. Perform. 29 (2020) 3233–3242.